

Terminal Atom-Controlled Etching of 2D-TMDs

Ziwei Huang, Wei Deng, Zhengwei Zhang, Bei Zhao, Hongmei Zhang, Di Wang, Bailing Li, Miaoqiao Liu, Ying Huangfu, and Xidong Duan*

The controlled etching of 2D transition metal dichalcogenides (2D-TMDs) is critical to understanding the growth mechanisms of 2D materials and patterning 2D materials but remains a major comprehensive challenge. Here, a rational strategy to control the terminal atoms of 2D-TMDs etched holes is reported. Using laser irradiation combined with an improved anisotropic thermal etching process under a determined atmosphere, terminal atom-controlled etched hole arrays are created on 2D-TMDs. By adjusting the gas atmosphere during the thermal etching stage, triangular etched hole arrays terminated by the tungsten zigzag (W-ZZ) edge (in an Ar/H₂ atmosphere), hexagonal etched hole arrays terminated alternately by the W-ZZ edge and sulfur (selenium) zigzag (S-ZZ or Se-ZZ) edge (in a pure Ar atmosphere), and triangular etched hole arrays terminated by the S-ZZ (Se-ZZ) edge (in an Ar/sulfur [selenium] vapor atmosphere) can be obtained. Density functional theory reveals the forming energy of different edges and the different activities of metal atoms and chalcogenide atoms under different atmospheres, which determine the terminal atoms of the holes. This work may enhance the understanding of the etching and growth of 2D-TMDs. The 2D-TMDs hole arrays constructed by this work may have important applications in catalysis, nonlinear optics, spintronics, and large-scale integrated circuits.

1. Introduction

In recent years, atomically thin 2D layered materials, such as graphene, ultrathin hexagonal boron nitride (hBN), transition metal dichalcogenides (TMDs), and black phosphorus,

have attracted extensive attention because of their fascinating physical and chemical properties.^[1–10] In particular, due to their unique crystal structure and fascinating physical and chemical properties, 2D-TMDs have promising applications in electronics, optoelectronics, spintronics, catalysis, etc.^[11–15] To date, a variety of high-quality, large-area, even wafer-scale single-crystal atomic thin films of 2D-TMDs (e.g., MoS₂ and WS₂) have been obtained through the chemical vapor deposition (CVD) method.^[16–22] However, the growth mechanism of 2D-TMDs has always been an important subject that we are eager to clarify, which has yet to be fully revealed and is still a great challenge to researchers. For example, Tang et al. set forth the growth mechanism of 2D-TMDs by analyzing typical heterogeneous nucleation reactions.^[23] Yang et al. observed the formation of 2D transition metal oxide nanosheets by in situ transmission electron microscopy and revealed the growth process of 2D materials to a

certain extent.^[24] Despite considerable efforts and research, the growth mechanism has not been discussed entirely to reveal the growth process fully. It is noteworthy that etching (a widely used processing technology in the industry) as a reverse growth process is of great significance in studying material growth mechanisms and has been widely studied to reveal many material growth mechanisms.^[25,26]

In contrast to crystal growth, in which atoms are epitaxy at the front edges (planes) of the material, etching mainly removes atoms around the edges or defects of a 2D material. According to the kinetic Wulff construction, it will generate edges with different growth rates during the growth process of 2D-TMDs, and eventually the fast-growth edges (planes) will disappear, and only slow-growth edges (planes) will remain.^[27–29] During the etching process of 2D-TMDs, there also exist edges with different etching rates, and the materials will terminate on edges with slower etching rates, which should be inconsistent with the etching process of graphene. It is worth mentioning that the edge structure of 2D-TMD crystals profoundly affects their properties.^[30,31] Therefore, it is of great significance to study the etching process of 2D-TMDs with controllable etching parameters, such as gas atmosphere, etching time, and etching temperature, during the etching process and to achieve 2D-TMD nanostructures with regular crystal edge structures.

Z. Huang, W. Deng, H. Zhang, D. Wang, B. Li, M. Liu,
Y. Huangfu, X. Duan

Hunan Provincial Key Laboratory of Two-Dimensional Materials
State Key Laboratory for Chemo/Biosensing and Chemometrics
College of Chemistry and Chemical Engineering
Hunan University
Changsha 410082, China
E-mail: xidongduan@hnu.edu.cn

Z. Zhang
Hunan Key Laboratory of Super-microstructure and Ultrafast Process
School of Physics and Electronics
Central South University
Changsha 410083, China

B. Zhao
School of Physics and Key Laboratory of MEMS of Ministry of Education
School of Physics
Southeast University
Nanjing 211189, China

 The ORCID identification number(s) for the author(s) of this article can be found under <https://doi.org/10.1002/adma.202211252>.

DOI: 10.1002/adma.202211252

The etching of 2D materials may also have engineering applications. The 2D materials with atomically thin holey arrays have shown exciting applications in photonics. For example, Zhang et al. reported an optical waveguide device prepared by monolayer holey WS₂ scaling down optical devices, which is several orders of magnitude smaller than today's devices, leading to higher density and higher capacity photonic chips.^[32] 2D materials with atomically thin holey arrays can provide a platform for synthesizing patterned heterostructures. Recently, Zhang et al. reported using 2D-TMDs with etching hole arrays as templates and achieving highly robust endoepitaxial growth of monolayer lateral heterostructure arrays, which marks a critical step in the large-scale integration of 2D semiconductor heterostructures.^[33]

Some studies on the etching of 3D crystal materials or 2D materials have been extensively reported in recent years, and the methods of etching have varied. For example, Yang et al. reported anisotropic etching of graphene using hydrogen plasma, and Zhao et al. used a co-etching method with oxygen plasma and ozone to construct nanopores on graphene, which pushed the etching of 2D materials to a new height and provided ideas for follow-up research.^[34,35] Nevertheless, as a common etching method, hydrogen (oxygen) plasma etching will damage the part of the materials that do not need to be etched to a certain extent, which limits the practical application to some extent. Battulga Munkhbat et al. reported an etching process of 2D-TMDs that combines standard top-down lithography nanofabrication with anisotropic wet etching, producing a regular array of hexagonal holes on 2D-TMDs.^[36] However, complex lithography processes may introduce residual photoresist, resulting in unclean surface and hole edges of materials after the etching process, while the damage of the unetched area of the 2D materials caused by the aqueous etchant solution was not assessed in this work. Li et al. reported the etching of monolayer MoS₂ domains by oxygen.^[37] In this work, the hole arrangement is random and disordered, and a large number of oxidized particle points are observed in the pore edge region, which is unfavorable for subsequent applications. In summary, finding a general etching method for large-scale clean etching and controlling the terminal edge atoms and thus the direction and shape of etching holes on atomically thin 2D materials remains challenging.

Here, we report the terminal atom-controlled etching of 2D-TMDs (e.g., WS₂, WSe₂, or MoS₂) with atomically clean hole edges through defects introduced by laser irradiation in air and subsequent thermal etching in a controlled etching atmosphere (i.e., a hydrogen atmosphere, inert atmosphere, and sulfur [selenium] vapor atmosphere). With integrated differential phase contrast scanning transmission electron microscopy (iDPC-STEM) analysis and microscopy images of the etched holes combined with atomic model analysis, we confirmed that the triangular holes etched in an argon-hydrogen mixture atmosphere (Ar/H₂, see the Experimental Section) are terminated by the tungsten zigzag (W-ZZ) edge, the triangular holes etched in sulfur (selenium) vapor and argon mixture atmosphere (Ar/sulfur [selenium] vapor, see the Experimental Section) are terminated by the sulfur (selenium) zigzag (S-ZZ or Se-ZZ) edge, and the hexagonal holes etched in an inert atmosphere (pure Ar, see the Experimental Section) are terminated

alternately by the W-ZZ edge and S-ZZ (Se-ZZ) edge. When the terminal atoms of the original etched 2D-TMDs are fixed, the shape and direction of the etched hole arrays are 100% determined (see the following). Meanwhile, the unetched region retains its intrinsic crystal structure, which indicates that rapid thermal etching is non-destructive to this part of the material. This work provides a new method for etching 2D-TMD materials with atomically clean and determined terminal atom edges and thus provides a new idea in many chemistry and electronics areas. For example, since etching is a reverse reaction process of growth, controlled etching in different atmospheres provides a new idea for clarifying the mechanism of CVD synthesis of 2D materials. More importantly, the etched hole array structure can be used for epitaxial other 2D materials, which lays the foundation for large-scale and high-density integration of heterostructures.^[33] Only the edge atoms are always the catalytic active points when 2D-TMDs are utilized as catalysts for some chemical reactions.^[38,39] To improve the catalytic activity, producing many pores in 2D-TMDs to expose more edges is needed. The terminal atom type will affect the final catalytic activity in this situation. Therefore, this work provides a way to study and modify the catalysis of 2D-TMDs.

2. Result and Discussion

Figure 1 schematically illustrates the etching process, including defect arrays produced through laser irradiation in air and high-temperature thermal etching of 2D-TMDs at a high temperature under a certain atmosphere. According to previous studies, CVD-grown WS₂ single crystals should always be terminated by the most stable W-ZZ edge or S-ZZ edge, which similarly applies to stable etching holes.^[40–43] For simplicity, we focus our discussion on the etching of monolayer 2H WS₂ terminated by the S-ZZ edge unless otherwise mentioned (see Figure S1, Supporting Information, to determine the terminal atoms of monolayer WS₂ used in the work). The growth of large-area monolayer WS₂ through the mature double-flow CVD method is similar to previous work.^[44] A combination of focused laser irradiation and raster scanning under a confocal Raman microscope (see the Experimental Section) was used to form periodic defect arrays on monolayer WS₂ (each defect is \approx 300–400 nm in size, Figure S2, Supporting Information). Then thermal etching was performed at controlled temperatures, atmospheres, and durations to produce periodic etched hole arrays in the WS₂ crystal.^[33,45]

To realize periodic etching, periodic point defects were produced using laser irradiation in air. Generally, etching occurs more easily at defects. It is necessary to establish a critical equilibrium to vaporize the atoms around the laser irradiation spots selectively and ensure that the unetched areas are absolutely non-destructive. To meet these conditions, we created a method of a thermal etching by pushing the sample into a high-temperature tubular furnace for a while and pulling it out to cool down (see Figure S3, Supporting Information, and Experimental Section for details). It is worth noting that when argon and hydrogen (or pure argon) were used directly as carrier gases in the thermal etching process, the sample was thermally etched with a silicon substrate face up (Figure S3c, Supporting

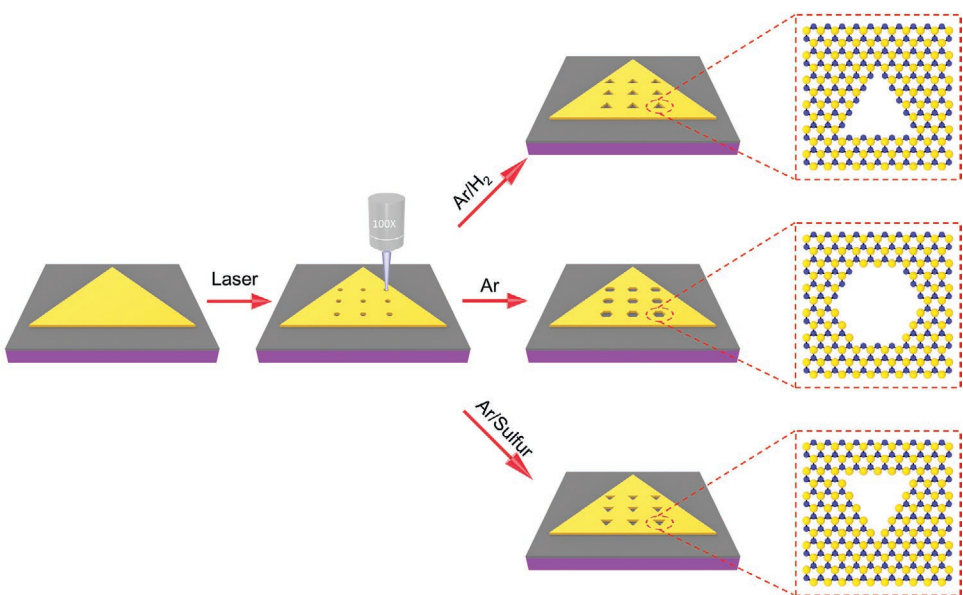


Figure 1. Schematic illustration of controlled etching on TMDs. Monolayer 2H WS₂ terminated by S-ZZ was taken as the object to expound. Monolayer WS₂ single crystals are first obtained by chemical vapor deposition (CVD). A laser confocal Raman microscope was used to prepare point defect arrays on a selected monolayer triangle WS₂ domain. The high-temperature (1000 °C) annealing process can take three forms, as shown in the figure. In an atmosphere mixed with argon and hydrogen, WS₂ with periodic forward (consistent with the triangular orientation of WS₂) triangular etched hole arrays was produced. In a pure argon atmosphere, WS₂ with periodic hexagonal etched hole arrays was produced. In an atmosphere mixed with argon and sulfur vapor, WS₂ with periodic reverse (oriented 180° with triangular WS₂) triangular etched hole arrays was produced.

Information). When the sulfur (selenium) vapor and argon mixture were used as an etching atmosphere, sulfur (selenium) powder was used as a solid source to provide stable sulfur (selenium) vapor. In this regard, we created a microcavity by diagonally placing the sample face down above the sulfur (selenium) powder (Figure S3d, Supporting Information). In this microcavity, the sulfur (selenium) powder provides a stable sulfur (selenium) atmosphere to produce the etched hole arrays.

More importantly, we noticed that when the etching process is conducted in Ar/H₂, the obtained triangular etched hole arrays are always parallel to the template material, which we defined as forward etched hole arrays (FHAs). Nevertheless, when etching occurs in Ar/sulfur vapor, the obtained triangular etched hole arrays always have an angle of 180° to the template material, which we defined as reverse etched hole arrays (RHAs). When the etching process is performed in Ar, hexagonal etched hole arrays are obtained, which we defined as hexagonal hole arrays (HHAs). As mentioned above, the 2H WS₂ terminated by the S-ZZ edge is the object of our study, while the orientation difference between W-ZZ and S-ZZ is 60° or 180°. Based on this, we can infer from the atomic structure that the edges of the forward triangular etched hole etching in Ar/H₂ are terminated by the W-ZZ edge (Figure S4a, Supporting Information). Similarly, we can infer the reverse triangular etched hole obtained by sulfur vapor-induced thermal etching terminated by S-ZZ edges (Figure S4c, Supporting Information). The hexagonal etched hole obtained by thermal etching in Ar has three sides parallel to the forward triangular etched hole, while the other three sides are parallel to the reverse triangular etched hole, so it can be inferred that the edges of the hexagonal etched hole terminated alternately by the W-ZZ edge and S-ZZ edge (Figure S4b, Supporting Information).

Figure 2a,e,i shows three typical optical microscopy (OM) images of monolayer WS₂ single crystals supported by SiO₂/Si substrates after defect induction through laser irradiation and thermal etching under high temperature and in different atmospheres. We also collected low magnification OM images to better distinguish FHAs and RHAs (Figure S5, Supporting Information). In previous studies on the etching of 2D materials, for example, etching of 2D-MoS₂ in oxygen or etching of 2D-hBN in nitrogen, the shape of the etched holes was random and uncontrolled.^[46,47] However, in our work, the shape of the etched holes is fully controlled, resulting in 100% FHAs (Figure 2a), HHAs (Figure 2e), or RHAs (Figure 2i). In this regard, we calculated statistics on the shape of the holes obtained under different gas atmospheres (Figure S6, Supporting Information, and Experimental Section). Atomic force microscopy (AFM) studies demonstrated that the FHAs, HHAs, and RHAs were regularly arranged with a line profile height of ≈0.65 nm, consistent with monolayer WS₂ (Figure 2b,f,j). A scanning electron microscopy (SEM) study of three kinds of holey monolayer WS₂ (Figure 2c,g,k) corresponding to Figure 2a,e,i shows a number of well-defined etched hole arrays. The bright regions are the SiO₂/Si substrate, while the dark regions are monolayer WS₂. The Raman mapping images (Figure 2d,h,l) of monolayer WS₂ with three kinds of hole arrays at 357 cm⁻¹ which in agreement with the E_{2g}¹ in-plane resonance mode show characteristic Raman property of monolayer WS₂ in the unetched regions and a complete absence of the relevant signals in the etched hole regions. The Raman studies demonstrate that the complete removal of WS₂ in the hole regions and the resulting holey WS₂ retains a high crystalline and optical quality. The hole size shows a linear relationship with etching time (Figure 2m), corresponding OM images see Figure S7, Supporting Information. The etching

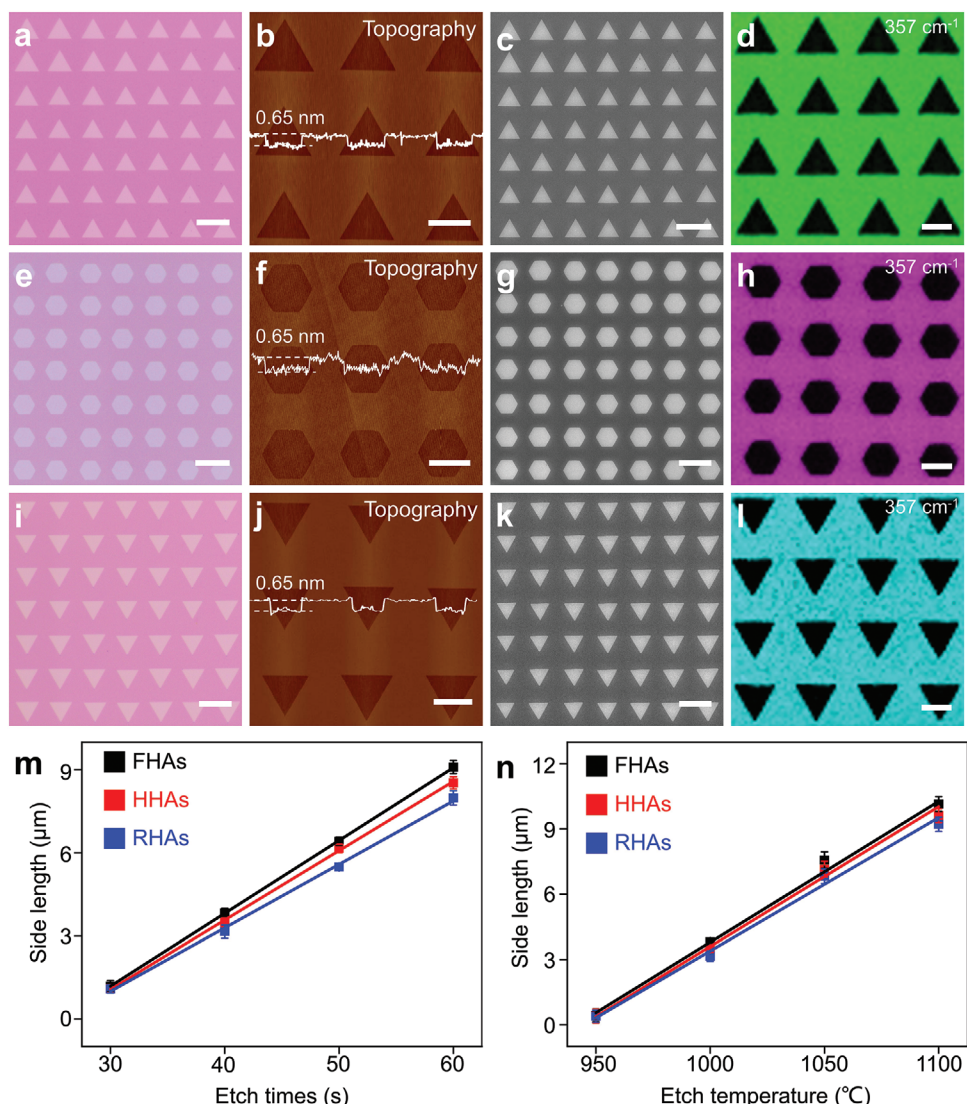


Figure 2. A variety of etched hole arrays on monolayer WS₂. a,e,i) Optical microscopy (OM) images of monolayer WS₂ with FHAs (a), HHAs (e), and RHAs (i). b,f,j) The corresponding AFM images of three kinds of holey WS₂. The line profiles in the three images all show a step height of 0.65 nm. c,g,k) The corresponding SEM images of three kinds of holey WS₂. d,h,l) Raman mapping image of three kinds of holey WS₂ at 357 cm⁻¹. m) The size of FHAs, HHAs, and RHAs as a function of the etching time at 1000 °C. n) The size of the FHAs, HHAs, and RHAs as a function of the etching temperature at a fixed etching duration of 40 s. Scale bars: 10 μm (a,c,e,g,i,k), 5 μm (b,f,j,d,h,l).

rates are about 0.26 (FHAs), 0.25 (HHAs), and 0.23 μm s⁻¹ (RHAs), respectively. The etching rate of monolayer WS₂ etched in Ar/H₂ is slightly higher than that in Ar while in Ar/sulfur vapor it is slightly lower, indicating that hydrogen can promote thermal etching and sulfur vapor can inhibit thermal etching, to a certain extent. And the etching rates can also be tuned by the etching temperature (Figure 2n and Figure S8, Supporting Information), demonstrating a highly robust and controllable etching process. In particular, for the etching of RHAs, the amount of sulfur powder is critical. Excessive or insufficient amount of sulfur powder will affect the thermal etching process (Figure S9, Supporting Information). In addition, etched hole arrays with various arrangement angles can be realized (e.g., 5° and 10°, Figure S10, Supporting Information) by inducing defect points with different arrangement angles by laser irradiation.

To further determine the boundary structure of the etched holes on monolayer WS₂, iDPC-STEM tests were performed on a WS₂ monolayer with a forward triangular etched hole, hexagonal etched hole, and reverse triangular etched hole. Meanwhile, we used STEM image simulations, corresponding to the iDPC-STEM characterization results, to illustrate the terminal atom arrangement at the edge of the three kinds of holes. Figure 3a,d,g shows low-magnification dark-field images of forward triangular etched hole etching in a hydrogen atmosphere, hexagonal etched hole etching in an argon atmosphere, and reverse triangular etched hole etching in a sulfur-vapor atmosphere, respectively. The holes' original shape and boundary were completely preserved after transferring. The edges of the holes are atomically sharp and have well-defined atomic terminations, while unetched regions have no defects and retain

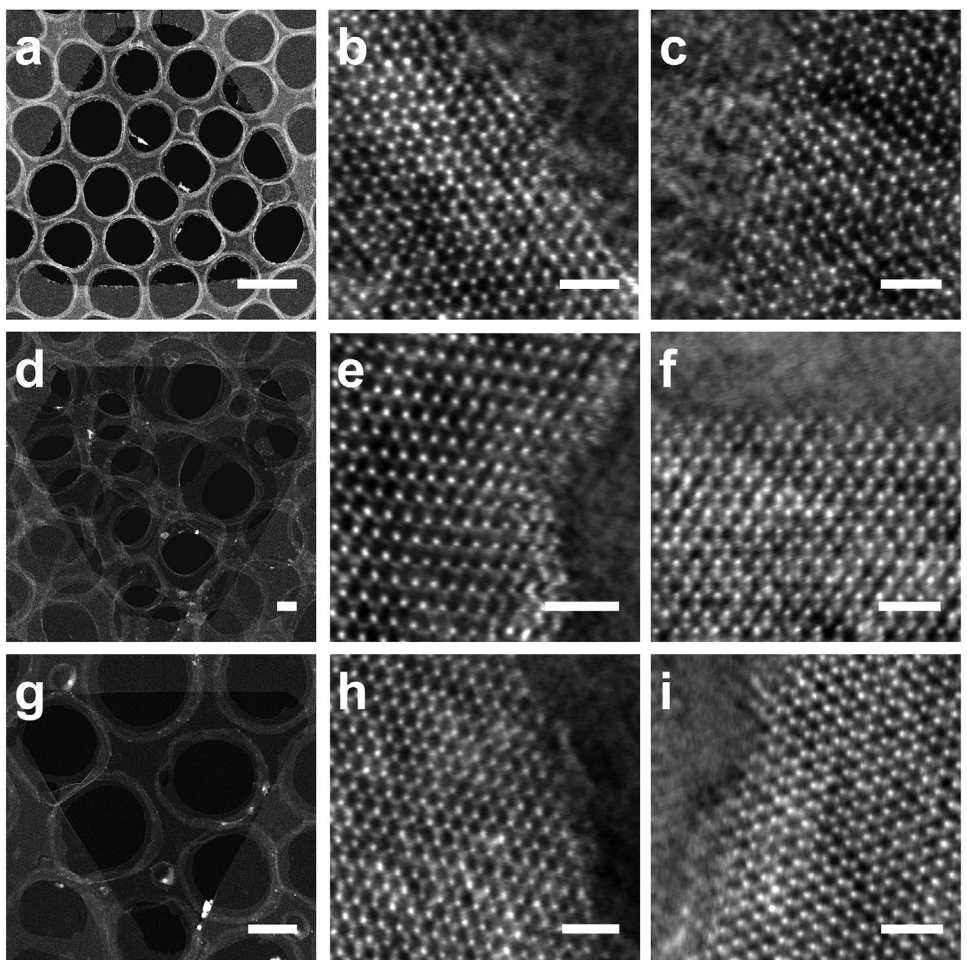


Figure 3. Atomic-resolution iDPC-STEM image of the boundary of three shaped holes. a) Low-magnification dark-field image of the forward triangular etched hole. b,c) Atomic-resolution Z-contrast iDPC-STEM image of two adjacent boundaries of the forward triangular etched hole. d) Low-magnification dark-field image of the hexagonal etched hole. e,f) Atomic-resolution Z-contrast iDPC-STEM image of two adjacent boundaries of the hexagonal etched hole. g) Low-magnification dark-field image of the reverse triangular etched hole. h,i) Atomic-resolution Z-contrast iDPC-STEM image of two adjacent boundaries of the reverse triangular etched hole. Scale bars: 1 μm (a,d,g), 1 nm (b,c,e,f,h,i).

the original high-quality crystal structure. Figure 3b,c shows the iDPC-STEM Z-contrast images corresponding to the two neighbor edges of the forward triangular etched hole shown in Figure 3a, in which W and S atoms can be clearly distinguished (W atoms are brighter dots while S atoms are darker dots). A clear hexagonal lattice structure of 2H WS₂ can be observed, demonstrating a nearly perfect lattice structure in the unetched WS₂ region with atomically smooth W-ZZ terminations on both edges. Some edges cannot be completely resolved due to the inevitable organic residue during wet transfer, but the atomic termination edge can be inferred from the hexagonal lattice structure near the hole edge region. The typical 2H WS₂ hexagonal lattice with W-ZZ and S-ZZ termination differs from a rotation angle of 60° or 180° (Figure S11, Supporting Information), while the edge of the etched hole must terminate with a stable zigzag structure. Therefore, atomic termination at the hole's edge can be inferred as long as the atomic lattice is arranged near the hole's edge. The iDPC-STEM Z-contrast images collected from the adjacent sides of the hexagonal etched hole show a W-ZZ termination edge and S-ZZ termination edge

(Figure 3e,f), consistent with a previous report.^[47] Similarly, iDPC-STEM Z-contrast images collected from two edges of the reverse triangular etched hole in Figure 3g (Figure 3h,i) show the complete lattice structure of the 2H WS₂ terminated by the S-ZZ edge. The terminal atoms of three kinds of holes are well defined, confirming the inference that the forward triangular etched hole etching in Ar/H₂ was terminated by the W-ZZ edge, the hexagonal etched hole etching in Ar was terminated alternately by the W-ZZ edge and S-ZZ edge, and the reverse triangular etched hole etching in Ar/sulfur vapor was terminated by the S-ZZ edge. By tuning the gas atmosphere during the thermal etching process, the terminal atoms of the holes in the WS₂ monolayer can be controlled, controllably resulting in etching monolayer WS₂ with 100% FHAs, HHAs, and RHAs.

We conducted density functional theory (DFT) calculations to explore the thermal etching mechanism of monolayer WS₂ in different atmospheres at laser irradiation-induced defect sites (see the Experimental Section for the specific calculation process). Figure 4a-c shows the formation energy change profile of three kinds of holes' edges in pure Ar (Figure 4a), in

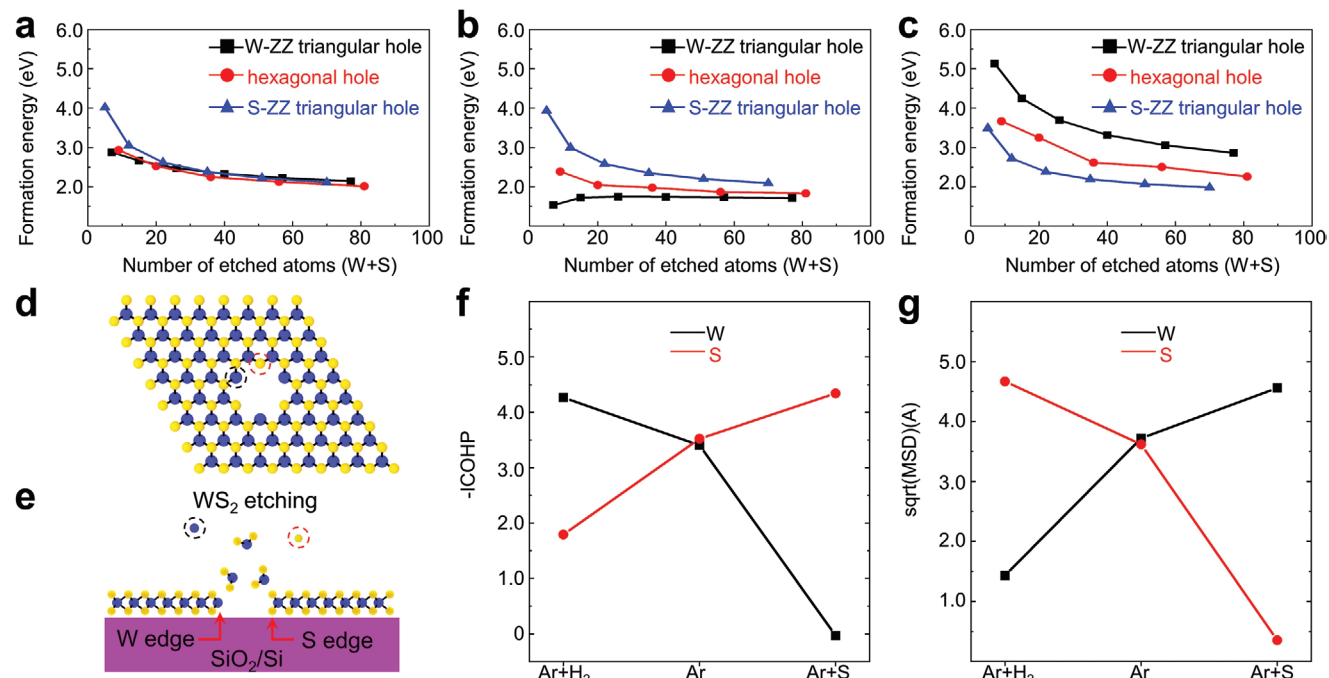


Figure 4. DFT theoretical calculations of the etching process. a-c) Formation energy change profile of the etching process of different kinds of holes' edges in pure Ar (a), in H₂ (b), and in S vapor (c). d) Schematic of the etching of monolayer WS₂ with point defects (top view) used to calculate the COHP of W atoms and S atoms. e) Schematic of the etching of monolayer WS₂ with point defects (front view) used to calculate the MSD of W atoms and S atoms. f) -ICOHP of W atoms and S atoms at the edge of point defect under different gas atmospheres. g) MSD of W atoms and S atoms at the edge of the point defect under different gas atmospheres.

H₂ (Figure 4b), and in sulfur vapor during the etching process (Figure 4c). The lower the formation energy value, the easier it is for this type of hole to form. To further illustrate the effect of different atmospheres on the formation energy of the edges of the holes, in particular, we calculate the formation energy change profile under a vacuum environment, as shown in Figure S11, Supporting Information. It can be seen that under a vacuum environment, the formation energy of W-ZZ edge is close to that of S-ZZ edge, indicating that W-ZZ edge and S-ZZ edge exist simultaneously during the etching process (Figure S12, Supporting Information). And in the case of the same hole area, the hexagonal hole has fewer edge sites than the triangle hole. To sum up, the hole etched in a vacuum environment is a hexagonal hole terminated alternately by W-ZZ edge and S-ZZ edge. In pure Ar atmosphere (Figure 4a), Ar atoms do not interact with the edge sites of W atoms or S atoms, so in the Ar atmosphere it is similar to the vacuum situation (the etched hole is a hexagonal hole terminated alternately by W-ZZ edge and S-ZZ edge). In H₂ atmosphere (Figure 4b), the W atom edge sites show a strong interaction with H₂, while the S atom edge sites are weaker, making the formation energy of W-ZZ edge much lower than that of S-ZZ edge. Therefore, in H₂ atmosphere, the W-ZZ edge is more stable, resulting in the etched hole terminated by the W-ZZ edge. In S atmosphere (Figure 4c), the W atom edge sites can combine with S atoms and spontaneously transform into S atom edge sites, which increases the chemical potential of W atom sites and leads to the formation energy of the W-ZZ edge being much bigger than the S-ZZ edge. Therefore, only the S-ZZ edge can exist stably during the etching process, leading to the etched hole terminated by the S-ZZ edge.

Figure 4d shows the atomic structure model of monolayer WS₂ in the early stage of thermal etching (top view), while Figure 4e shows the atomic structure model of monolayer WS₂ in the process of thermal etching (side view) and the atomization diffusion model. Thermal etching begins from the point defect site formed by laser irradiation and forms an etching hole along the lattice direction. First, we use CodeLobster to perform COHP (crystal orbital Hamilton population) and -ICOHP (integrate crystal orbital Hamilton population) calculations on the edge W atoms (marked by blue dots in Figure 4d) and S atoms (marked by yellow dots in Figure 4e) to investigate the bonding properties (Figure 4f and Figure S13, Supporting Information). The ICOHP value represents the binding strength, and a larger value indicates a greater bonding strength of atoms. Then, we used optimized structures to carry out ab initio molecular dynamics (AIMD) at a temperature of 1300 K under the NVT ensemble using a Nose-Hoover thermostat for 3000 fs with a time step of 1 fs, investigating the mean square displacement (MSD) of W atoms (marked by blue dots in Figure 4e) and S atoms (marked by yellow dots in Figure 4e) in different atmospheres (Figure 4g and Figure S14, Supporting Information). According to the calculation results shown in Figure 5f,g, in an Ar/H₂ atmosphere, the binding strength of S atoms is smaller than that of W atoms, and the MSD of S atoms is larger, so S atoms are easier to desorb during the thermal etching process, and the etched hole terminated by the W-ZZ edge eventually forms a forward triangular etched hole. In particular, in the pure Ar atmosphere, the binding strength of S atoms is almost the same as that of W atoms, while the MSDs of both kinds of atoms are close, indicating that the gasification degree of both

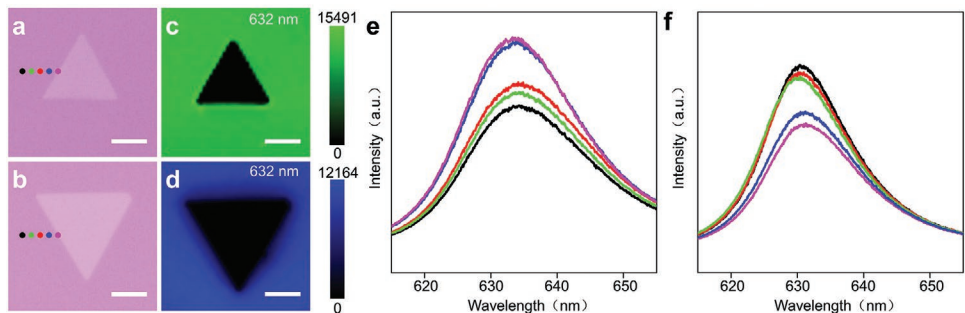


Figure 5. PL spectra of holes of monolayer WS_2 with different terminal atoms. a) OM image of triangle hole terminated by W-ZZ. b) OM image of triangle hole terminated by S-ZZ. c) PL mapping image of triangle hole terminated by W-ZZ at 632 nm. d) PL mapping image of triangle hole terminated by S-ZZ at 632 nm. e,f) The PL spectra for the locations as marked in (a) and (b), respectively. All scale bars are 5 μm .

atoms is nearly the same in the process of thermal etching, and finally, the etched hole is terminated by both the W-ZZ edge and S-ZZ edge, forming a hexagonal etched hole. In an Ar/sulfur vapor atmosphere, sulfur vapor supply effectively inhibits S atoms' desorption; in this case, the binding force of S atoms is greater than that of W atoms, and the MSD of S atoms is smaller. Eventually, the etched hole is terminated by the S-ZZ edge, forming a reverse triangular etched hole.

In general, different gas atmospheres determine the desorption capacity of W and S atoms, and ultimately, the terminal atoms of the etched holes can be controlled, which is consistent with the experimental results and further proves that it is reliable to control the terminal atoms of etched holes by regulating the thermal etching atmosphere.

According to previous work, different terminal atoms can profoundly affect photoluminescence (PL) properties of WS_2 .^[37,48,49] We have thus conducted PL spectroscopy and mapping studies to examine variation of PL intensity with different edges of the holes (Figure 5). Figure 5a,b shows the OM images of the triangle holes of monolayer WS_2 terminated by W-ZZ (Figure 5a) etched in Ar/H₂ and triangle holes terminated by S-ZZ (Figure 5b) etched in Ar/sulfur vapor. The blank areas are the exposed SiO₂/Si substrate after etching and the lavender areas are monolayer WS_2 . The corresponding PL mapping (Figure 5c,d) shows a strong PL signal at 632 nm (the near band-edge emission of monolayer WS_2) in the unetched region and no associated signal in the hole region, indicating that the hole has been completely etched.^[50] In particular, a significant lightened PL was observed at the hole edge terminated by W-ZZ (Figure 5c). The PL spectra taken at different locations in the WS_2 region (points marked in Figure 5a) confirm an increase in PL intensity at the hole edge compared to the unetched region (Figure 5e). This is because there more S vacancies are formed in the hole edge region during the etching processing under Ar/H₂ atmosphere. Nan et al., reported that the binding energy of an O₂ molecule on a S vacancy is much greater contrast to it on an ideal TMDs crystal, indicating that O₂ molecules are more likely to be absorbed on the S vacancy and it could be considered as chemisorbed.^[51] Due to the chemisorption of oxygen atoms on the S vacancies and the formation of partial W–O bonds with W atoms, resulting in the enhancement of PL intensity at the hole edges.^[52,53] Nonetheless, as shown in Figure 5d, a darkened PL was observed at the hole edge terminated by S-ZZ. And the PL spectra taken at different locations in the

WS_2 region (points marked in Figure 5b) show a decrease in PL intensity at the hole edge regions (Figure 5f). Similarly, the edge region of the hole terminated by S-ZZ has more W vacancies than the unetched region that leads to a decrease in the PL intensity, which is consistent with the conclusion of the previous report on the spatial non-uniformities of PL in monolayer WS_2 .^[54] The obtained etched hole edges terminating atoms can be perfectly regulated by controlling the atmosphere during the thermal etching process. And more importantly, their PL intensity can be effectively modulated, which lays the foundation for their future applications.

In addition, our approach can be extended to controllable etching of a wide range of 2D single crystals (e.g., WSe₂ and MoS₂). Similarly, monolayer WSe₂ and MoS₂ were irradiated by laser-induced defect arrays, and rapid etching occurred at high temperatures in different gas atmospheres. Figure 6a₁,b₁,c₁ shows OM images of monolayer WSe₂ with three kinds of hole arrays after etching in different gas atmospheres (i.e., FHAs in an Ar/H₂, HHAs in a pure Ar, and RHAs in an Ar/selenium vapor). Similarly, we collected low magnification OM images to better distinguish FHAs and RHAs (Figure S15, Supporting Information). Raman mapping (Figure 6a₂,b₂,c₂, characteristic peak at 250 cm^{-1} corresponding to the A_{1g} resonance mode) images show characteristic Raman properties of monolayer WSe₂ in the unetched regions, while a complete absence of the relevant signals occurs in the etched hole regions.

Atomically resolved high-angle annular dark-field scanning transmission electron microscope (HAADF-STEM) Z-contrast images collected from the three types of monolayer WSe₂ holes confirm that a nearly perfect crystalline structure is retained in the unetched region with atomically smooth and defined atom zigzag termination (Figure S16, Supporting Information), that is, a forward triangular etched hole terminated by the W-ZZ edge, a reverse triangular etched hole terminated by the Se-ZZ edge, and a hexagonal etched hole terminated alternately by the W-ZZ edge and Se-ZZ edge, respectively, which is consistent with the results of WS_2 . Figure 6d₁,e₁,f₁ shows OM images of etched hole of monolayer MoS₂. Similarly, the results are consistent with the etching of monolayer WS_2 or WSe₂ (forward triangular etched hole in an Ar/H₂, hexagonal etched hole in a pure Ar and reverse triangular etched hole in an Ar/sulfur vapor). The Raman mapping at 405 cm^{-1} (A_{1g} mode of MoS₂, Figure 6d₂,e₂,f₂) images also confirmed the formation of monolayer holey MoS₂. The uniform Raman mapping images

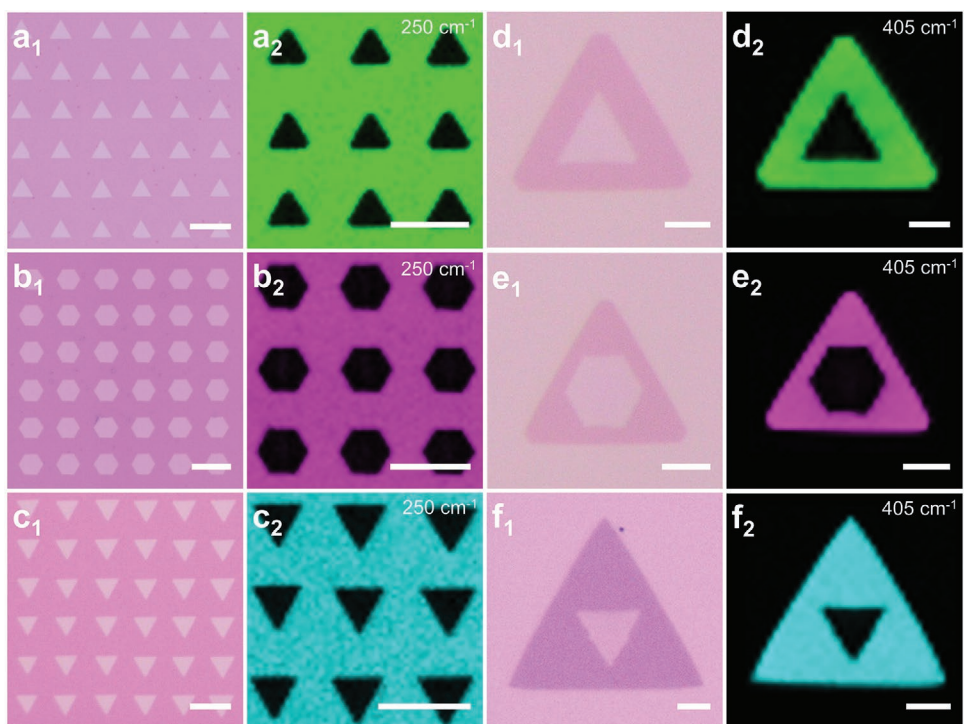


Figure 6. General terminal atom-controlled etching of 2D-TMDs. a₁,a₂) OM and Raman mapping images of monolayer WSe₂ with FHAs. b₁,b₂) OM and Raman mapping images of monolayer WSe₂ with HHAs. c₁,c₂) OM and Raman mapping images of monolayer WSe₂ with RHAs. d₁,d₂) OM and Raman mapping images of monolayer MoS₂ with a forward triangular etched hole. e₁,e₂) OM and Raman mapping images of monolayer MoS₂ with a hexagonal etched hole. f₁,f₂) OM and Raman mapping images of monolayer MoS₂ with a reverse triangular etched hole. All scale bars are 10 μm.

of both WSe₂ and MoS₂ indicate that the materials in the unetched regions are almost undamaged during rapid high-temperature thermal etching processes, which is undoubtedly of great significance for subsequent epitaxial growth or device preparation.

3. Conclusion

In summary, using a method combining inducing defects through laser irradiation in air and heat-induced etching in different atmospheres (e.g., hydrogen atmosphere, inert atmosphere, and sulfur [selenium] vapor atmosphere), we realized terminal atom controllable etching of 2D-TMDs (e.g., WS₂, WSe₂, and MoS₂) and further obtained controlled etched hole arrays (e.g., FHAs, HHAs, and RHAs). Detailed characterization demonstrates the formation of periodic hole arrays in 2D-TMDs (e.g., WS₂ and WSe₂), the etched holes have clear atomic terminations and atomic sharp edges, and the unetched 2D-TMDs retain high-quality crystalline. The PL characterizations proved that the PL intensity could be effectively regulated by well-defined terminal atoms obtained by thermal etching, which provided a new idea for studying 2D-TMDs material edges. 2D-TMDs with hole arrays can provide a suitable template for high-quality integrated optoelectronic devices. Furthermore, 2D-TMDs with terminal atom-controlled etched hole arrays or with terminal atom controllable edges may have significant application prospects in various fields, such as but not limited to catalysis, nonlinear optics, and spintronics.

4. Experimental Section

The Growth of Monolayer TMDs: In the tube furnace CVD system, monolayer WS₂, WSe₂, or MoS₂ were grown using a double-flow PVD process with an evaporation solid source. The powder (WS₂, WSe₂, or MoS₂, 3 g) was placed in a porcelain boat located in the central heating zone of the furnace, and a piece of silicon with 285 nm SiO₂ was placed downstream of the furnace as the growth substrate. The tube furnace was filled with ultrahigh purity argon (99.999%) for 3–5 min, and then the furnace with 70 sccm reflux argon was heated to 1200 °C under ambient pressure. After reaching the required growth temperature, the carrier gas was turned forward, the chemical vapor source went downstream, and the growth of monolayers occurred in 2–5 min for WSe₂ and 30 min for MoS₂. Then, the growth process was terminated, and the furnace was cooled naturally.

Induced Defect Array in 2D-TMDs through Direct Laser Irradiation in Air: A periodic defect array was generated on the monolayer TMDs (e.g., WS₂) by raster scanning of a focused laser beam with a programming pattern (488 nm 20 mW) under a confocal Raman microscope (Renishaw inVia) in air. The laser was CW laser. And the direction of polarization relative to the crystal was the same in all experiments. Each point defect was generated by exposure for \approx 5 s under a \times 100 objective lens (the approximate spot diameter was 0.98 μm and the laser power density was 2.58×10^6 W cm⁻²).

Rapid High-Temperature Thermal Etching: FHAs: The monolayer TMD sample with periodic defects (face up) was placed in a porcelain boat beside the heating zone, and the heating zone was kept at 1000 °C during the whole process. First, the central heating zone was purified with ultrahigh purity argon (99.999%) for 20 min. Then, the porcelain boat and the TMD sample were pulled into the central furnace heating zone using a quartz hook with two magnets. The carrier gas was changed to 200 sccm argon and 3 sccm hydrogen. Finally, the porcelain boat with TMD samples was pulled out, and the furnace was cooled naturally.

HHAs: The monolayer TMD sample with periodic defects (face up) was placed in a porcelain boat beside the heating zone, and the heating zone was kept at 1000 °C during the whole process. First, the central heating zone was purified with ultrahigh purity argon (99.999%) for 20 min. Then, the porcelain boat with the TMD sample was pulled into the central furnace heating zone, and the carrier gas was changed to 200 sccm argon. Finally, the porcelain boat with the TMD samples was pulled out, and the furnace was cooled naturally.

RHAs: 1 mg sulfur powder was placed in a porcelain boat beside the heating zone, the monolayer TMD sample with periodic defects (face down) was placed in the boat over the sulfur powder, and the heating zone was kept at 1000 °C during the whole process. First, the tube furnace was purified with ultrahigh purity argon (99.999%) for 20 min. Then, the porcelain boat with the TMD sample was pulled into the central furnace heating zone, and the carrier gas was changed to 200 sccm argon. Finally, the porcelain boat with the TMD samples out, and the furnace was cooled naturally.

Hole Shape Statistics: Ten monolayer WS₂ (each WS₂ irradiated 10 × 10 point arrays by the laser, with a total of 100 holes) etched in Ar/H₂, ten monolayer WS₂ etched in Ar, and ten monolayer WS₂ etched in Ar/sulfur vapor were counted. In Ar/H₂, the etched hole arrays were 100% HHAs. In Ar, the etched hole arrays were 100% RHAs. In Ar/sulfur vapor, the etched hole arrays were 100% RHAs.

STEM (TEM) Sample Preparation: The STEM (TEM) sample preparation method adopted improved wetting transfer technology (see Figure S17, Supporting Information). First of all, the silicon wafer with sample was spin coated with polymethyl methacrylate (PMMA) solution. The silicon wafer was observed carefully under a microscope to determine the location of the sample to be transferred. Then, a scalpel was used to cut a small square hole in the tape (the square hole should be slightly larger than the copper grid) and it was fitted on the silicon wafer. Afterward, the silicon wafer with sample to be transferred was placed in a 2 M NaOH solution and heated (100 °C) for 5–10 min. After the PMMA film with sample to be transferred was detached from the silicon wafer, it was rinsed with deionized water three to five times to remove the residual NaOH solution. Next the sample was transferred to prepared copper grid on the clean filter paper. To ensure a tight fit between the sample and the copper grid, a small amount of deionized water was added to the filter paper and then dried for about 10 min. After that, a small amount of acetone was added to dissolve the part where it was connected with the film and tape. Eventually, the copper grid with the transferred sample was placed in acetone solution for 2 h to remove all PMMA.

DFT Calculation Details: DFT calculations were performed using the Quantum Espresso based on the pseudopotential plane wave method.^[55,56] The Perdew–Burke–Ernzerhof functional was used to describe the exchange-correlation effects of electrons.^[57] The projected augmented wave potentials were chosen to describe the ionic cores and take valence electrons into account using a plane wave basis set with a kinetic energy cutoff of 500 eV.^[58,59] To simulate the substrate surface structure, a 4 × 4 × 1 WS₂ supercell containing a defect was built, and an extra vacuum zone of 12 Å was applied along the z-direction to avoid interactions between unit cells. An atmosphere of pure Ar gas, a mixture of Ar/H₂ ($n_{\text{Ar}}: n_{\text{H}_2} = 1:1$) gas, and a mixture of Ar/sulfur vapor ($n_{\text{Ar}}: n_{\text{S}} = 2:3$) gas was randomly added into the vacuum to describe the effects of different environments. All structures were first optimized to reach their most stable configuration. During the geometry optimizations, all the atom positions were allowed to relax. The optimized structures were then used to carry out AIMD at a temperature of 1300 K under the NVT ensemble using a Nose–Hoover thermostat for 3000 fs with a time step of 1 fs.^[60] To investigate the bonding properties, COHP calculations were carried out by CodeLobster.^[61,62] In this work, Brillouin-zone sampling was conducted using Monkhorst–Pack grids of special points with a separation of 0.04 Å⁻¹.^[63] The structure optimization convergence criterion for the electronic self-consistent field loop was set to 1×10^{-5} eV/atom.

The hole formation energy (E_F) was calculated through,

$$E_F = E_h + N_W \mu_W + N_S \mu_S - N_E \mu_{\text{atm}} - E_{\text{ref}} \quad (1)$$

where E_h was the energy of hole structure corroded N_W W atoms and N_S S atoms, μ_W and μ_S were energies of W and S atoms, N_E was the number of edge atoms of the hole, μ_{atm} was the chemical potential correction of the atmosphere which was obtained from the binding energy between edge atoms and H₂/Ar/S molecules, and E_{ref} was the energy of the reference (without hole) structure.

Characterization: The morphology and thickness of the 2D-TMDs with hole arrays were characterized by OM (DP27, Olympus), AFM (Biopore System, Bruker), and SEM (MIRA3 LMH, TESCAN). The Raman and PL spectra and mapping were obtained by a confocal microscope-based Raman system (inVia Reflex, Renishaw with a 488 nm laser as the excitation source). HAADF-STEM characterization was performed using a JEOL JEM-ARM200F (200 kV).

Supporting Information

Supporting Information is available from the Wiley Online Library or from the author.

Acknowledgements

Z.W.H. and W.D. contributed equally to this work. The authors acknowledge support from the National Natural Science Foundation of China (No. 51872086) and the Innovative Research Groups of Hunan Province (Grant 2020JJ1001).

Conflict of Interest

The authors declare no conflict of interest.

Data Availability Statement

The data that support the findings of this study are available from the corresponding author upon reasonable request.

Keywords

etched hole arrays, rapid thermal etching, terminal atom-controlled, two-dimensional transition metal dichalcogenides

Received: December 1, 2022

Revised: January 19, 2023

Published online: March 17, 2023

- [1] C. R. Dean, A. F. Young, I. Meric, C. Lee, L. Wang, S. Sorgenfrei, K. Watanabe, T. Taniguchi, P. Kim, K. L. Shepard, J. Hone, *Nat. Nanotechnol.* **2010**, *5*, 722.
- [2] K. Kang, K. H. Lee, Y. Han, H. Gao, S. Xie, D. A. Muller, J. Park, *Nature* **2017**, *550*, 229.
- [3] M. Y. Li, Y. Shi, C. C. Cheng, L. S. Lu, Y. C. Lin, H. L. Tang, M. L. Tsai, C. W. Chu, K. H. Wei, J. H. He, W. H. Chang, K. Suenaga, L. J. Li, *Science* **2015**, *349*, 524.
- [4] Y. Liu, X. Duan, H.-J. Shin, S. Park, Y. Huang, X. Duan, *Nature* **2021**, *591*, 43.
- [5] B. Radisavljevic, A. Radenovic, J. Brivio, V. Giacometti, A. Kis, *Nat. Nanotechnol.* **2011**, *6*, 147.
- [6] J. R. Schaibley, H. Yu, G. Clark, P. Rivera, J. S. Ross, K. L. Seyler, W. Yao, X. Xu, *Nat. Rev. Mater.* **2016**, *1*, 16055.

- [7] L. Wang, X. Xu, L. Zhang, R. Qiao, M. Wu, Z. Wang, S. Zhang, J. Liang, Z. Zhang, Z. Zhang, W. Chen, X. Xie, J. Zong, Y. Shan, Y. Guo, M. Willinger, H. Wu, Q. Li, W. Wang, P. Gao, S. Wu, Y. Zhang, Y. Jiang, D. Yu, E. Wang, X. Bai, Z.-J. Wang, F. Ding, K. Liu, *Nature* **2019**, *570*, 91.
- [8] Q. H. Wang, K. Kalantar-Zadeh, A. Kis, J. N. Coleman, M. S. Strano, *Nat. Nanotechnol.* **2012**, *7*, 699.
- [9] Z. Wu, Y. Lyu, Y. Zhang, R. Ding, B. Zheng, Z. Yang, S. P. Lau, X. H. Chen, J. Hao, *Nat. Mater.* **2021**, *20*, 1203.
- [10] H. Zhu, Y. Wang, J. Xiao, M. Liu, S. Xiong, Z. J. Wong, Z. Ye, Y. Ye, X. Yin, X. Zhang, *Nat Nanotechnol* **2015**, *10*, 151.
- [11] M. Chhowalla, H. S. Shin, G. Eda, L. J. Li, K. P. Loh, H. Zhang, *Nat. Chem.* **2013**, *5*, 263.
- [12] D. Deng, K. S. Novoselov, Q. Fu, N. Zheng, Z. Tian, X. Bao, *Nat. Nanotechnol.* **2016**, *11*, 218.
- [13] K. F. Mak, J. Lee, C. F. Hone, J. Hone, J. Fau – Shan, T. F. Shan, J. F. Heinz, T. F. Heinz, *Phys. Rev. Lett.* **2010**, *105*, 136805.
- [14] K. F. Mak, K. L. McGill, J. Park, P. L. McEuen, *Science* **2014**, *344*, 1489.
- [15] D. Voiry, H. Yamaguchi, J. Li, R. Silva, D. C. B. Alves, T. Fujita, M. Chen, T. Asefa, V. B. Shenoy, G. Eda, M. Chhowalla, *Nat. Mater.* **2013**, *12*, 850.
- [16] Y. Gao, Z. Liu, D. M. Sun, L. Huang, L. P. Ma, L. C. Yin, T. Ma, Z. Zhang, X. L. Ma, L. M. Peng, H. M. Cheng, W. Ren, *Nat. Commun.* **2015**, *6*, 8569.
- [17] K. Kang, S. Xie, L. Huang, Y. Han, P. Y. Huang, K. F. Mak, C. J. Kim, D. Muller, J. Park, *Nature* **2015**, *520*, 656.
- [18] T. Li, W. Guo, L. Ma, W. Li, Z. Yu, Z. Han, S. Gao, L. Liu, D. Fan, Z. Wang, Y. Yang, W. Lin, Z. Luo, X. Chen, N. Dai, X. Tu, D. Pan, Y. Yao, P. Wang, Y. Nie, J. Wang, Y. Shi, X. Wang, *Nat. Nanotechnol.* **2021**, *16*, 1201.
- [19] J. Shim, S.-H. Bae, W. Kong, D. Lee, K. Qiao, D. Nezich, Y. J. Park, R. Zhao, S. Sundaram, X. Li, H. Yeon, C. Choi, H. Kurn, R. Yue, G. Zhou, Y. Ou, K. Lee, J. Moodera, X. Zhao, J. H. Ahn, C. Hinkle, A. Ougazzaden, J. Kim, *Science* **2018**, *362*, 665.
- [20] J. Wang, X. Xu, T. Cheng, L. Gu, R. Qiao, Z. Liang, D. Ding, H. Hong, P. Zheng, Z. Zhang, Z. Zhang, S. Zhang, G. Cui, C. Chang, C. Huang, J. Qi, J. Liang, C. Liu, Y. Zuo, G. Xue, X. Fang, J. Tian, M. Wu, Y. Guo, Z. Yao, Q. Jiao, L. Liu, P. Gao, Q. Li, R. Yang, et al., *Nat. Nanotechnol.* **2021**, *17*, 33.
- [21] Q. Wang, N. Li, J. Tang, J. Zhu, Q. Zhang, Q. Jia, Y. Lu, Z. Wei, H. Yu, Y. Zhao, Y. Guo, L. Gu, G. Sun, W. Yang, R. Yang, D. Shi, G. Zhang, *Nano Lett.* **2020**, *20*, 7193.
- [22] X. Xu, Y. Pan, S. Liu, B. Han, P. Gu, S. Li, W. Xu, Y. Peng, Z. Han, J. Chen, P. Gao, Y. Ye, *Science* **2021**, *372*, 195.
- [23] L. Tang, J. Tan, H. Nong, B. Liu, H.-M. Cheng, *Acc. Mater. Res.* **2021**, *2*, 36.
- [24] J. Yang, Z. Zeng, J. Kang, S. Betzler, C. Czarnik, X. Zhang, C. Ophus, C. Yu, K. Bustillo, M. Pan, J. Qiu, L.-W. Wang, H. Zheng, *Nat. Mater.* **2019**, *18*, 970.
- [25] L. Cai, M. J. Shearer, Y. Zhao, Z. Hu, F. Wang, Y. Zhang, K. W. Eliceiri, R. J. Hamers, W. Yan, S. Wei, M. Tang, S. Jin, *J. Am. Chem. Soc.* **2018**, *140*, 10980.
- [26] T. He, Z. Wang, F. Zhong, H. Fang, P. Wang, W. Hu, *Adv. Mater. Technol.* **2019**, *4*, 1900064.
- [27] A. Vasilii, Y. Liu, I. Y. Boris, *Proc. Natl. Acad. Sci. U. S. A.* **2012**, *109*, 15136.
- [28] T. Ma, W. Ren, X. Zhang, Z. Liu, Y. Gao, L.-C. Yin, X.-L. Ma, F. Ding, H.-M. Cheng, *Proc. Natl. Acad. Sci. U. S. A.* **2013**, *110*, 20386.
- [29] H. Sun, J. Dong, F. Liu, F. Ding, *Mater. Today* **2021**, *42*, 192.
- [30] X. Yin, Z. Ye, A. C. Daniel, Y. Ye, K. O'Brien, C. H. James, X. Zhang, *Science* **2014**, *344*, 488.
- [31] W. Zhou, Z. Yin, Y. Du, X. Huang, Z. Zeng, Z. Fan, H. Liu, J. Wang, H. Zhang, *Small* **2013**, *9*, 140.
- [32] X. Zhang, C. De-Eknakul, J. Gu, A. L. Boehmke, V. M. Menon, J. Khurgin, E. Cubukcu, *Nat. Nanotechnol.* **2019**, *14*, 844.
- [33] Z. Zhang, Z. Huang, J. Li, D. Wang, Y. Lin, X. Yang, H. Liu, S. Liu, Y. Wang, B. Li, X. Duan, X. Duan, *Nat. Nanotechnol.* **2022**, *17*, 493.
- [34] R. Yang, L. Zhang, Y. Wang, Z. Shi, D. Shi, H. Gao, E. Wang, G. Zhang, *Adv. Mater.* **2010**, *22*, 4014.
- [35] J. Zhao, G. He, S. Huang, L. F. Villalobos, M. Dakhchoune, H. Bassas, K. V. Agrawal, *Sci. Adv.* **2019**, *5*, 1851.
- [36] B. Munkhbat, A. B. Yankovich, D. G. Baranov, R. Verre, E. Olsson, T. O. Shegai, *Nat. Commun.* **2020**, *11*, 4604.
- [37] J. Li, S. Hu, Z. Chen, Y. Liang, H. Kang, Y. Zhang, Y. Sui, S. Wang, G. Yu, S. Peng, Z. Jin, X. Liu, *Appl. Surf. Sci.* **2020**, *510*, 145412.
- [38] H. Li, Y. Tan, P. Liu, C. Guo, M. Luo, J. Han, T. Lin, F. Huang, M. Chen, *Adv. Mater.* **2016**, *28*, 8945.
- [39] H. Wang, X. Liu, P. Niu, S. Wang, J. Shi, L. Li, *Matter* **2020**, *2*, 1377.
- [40] P. Ruffieux, S. Wang, B. Yang, C. Sánchez-Sánchez, J. Liu, T. Dienel, L. Talirz, P. Shinde, C. A. Pignedoli, D. Passerone, T. Dumslaff, X. Feng, K. Müllen, R. Fasel, *Nature* **2016**, *531*, 489.
- [41] S. Wang, Y. Rong, Y. Fan, M. Pachios, H. Bhaskaran, K. He, J. H. Warner, *Chem. Mater.* **2014**, *26*, 6371.
- [42] Z. Wang, Q. Li, H. Xu, C. Dahl-Petersen, Q. Yang, D. Cheng, D. Cao, F. Besenbacher, J. V. Lauritsen, S. Helveg, M. Dong, *Nano Energy* **2018**, *49*, 634.
- [43] M. Yamamoto, T. L. Einstein, M. S. Fuhrer, W. G. Cullen, *J. Phys. Chem.* **2013**, *117*, 25643.
- [44] Z. Zhang, P. Chen, X. Duan, K. Zang, J. Luo, X. Duan, *Science* **2017**, *357*, 788.
- [45] J. Li, X. Yang, Y. Liu, B. Huang, R. Wu, Z. Zhang, B. Zhao, H. Ma, W. Dang, Z. Wei, K. Wang, Z. Lin, X. Yan, M. Sun, B. Li, X. Pan, J. Luo, G. Zhang, Y. Liu, Y. Huang, X. Duan, X. Duan, *Nature* **2020**, *579*, 368.
- [46] D. Lv, H. Wang, D. Zhu, J. Lin, G. Yin, F. Lin, Z. Zhang, C. Jin, *Sci. Bull.* **2017**, *62*, 846.
- [47] Y. Y. Stehle, X. Sang, R. R. Unocic, D. Voylov, R. K. Jackson, S. Smirnov, I. Vlassiok, *Nano Lett.* **2017**, *17*, 7306.
- [48] C. Cong, J. Shang, X. Wu, B. Cao, N. Peimyoo, C. Qiu, L. Sun, T. Yu, *Adv. Opt. Mater.* **2014**, *2*, 131.
- [49] Y. Sheng, X. Wang, K. Fujisawa, S. Ying, A. L. Elias, Z. Lin, W. Xu, Y. Zhou, A. M. Korsunsky, H. Bhaskaran, M. Terrones, J. H. Warner, *ACS Appl. Mater. Interfaces* **2017**, *9*, 15005.
- [50] H. R. Gutiérrez, N. Perea-López, A. L. Elías, A. Berkdemir, B. Wang, R. Lv, F. López-Urías, V. H. Crespi, M. Terrones, *Nano Lett.* **2013**, *13*, 3447.
- [51] H. Nan, Z. Wang, W. Wang, Z. Liang, Y. Lu, Q. Chen, D. He, P. Tan, F. Miao, X. Wang, J. Wang, Z. Ni, *ACS Nano* **2014**, *8*, 5738.
- [52] Z. Hu, J. Avila, X. Wang, J. F. Leong, Q. Zhang, Y. Liu, M. C. Asensio, J. Lu, A. Carvalho, C. H. Sow, A. H. C. Neto, *Nano Lett.* **2019**, *19*, 4641.
- [53] Z. Luo, W. Zheng, N. Luo, B. Liu, B. Zheng, X. Yang, D. Liang, J. Qu, H. Liu, Y. Chen, Y. Jiang, S. Chen, X. Zou, A. Pan, *Nano Lett.* **2022**, *22*, 2112.
- [54] H. Y. Jeong, Y. Jin, S. J. Yun, J. Zhao, J. Baik, D. H. Keum, H. S. Lee, Y. H. Lee, *Adv. Mater.* **2017**, *29*, 1605043.
- [55] P. Giannozzi, O. Andreussi, T. Brummel, O. Bunau, M. B. Nardelli, M. Calandra, R. Car, C. Cavazzoni, D. Ceresoli, M. Cococcioni, N. Colonna, I. Carnimeo, A. D. Corso, S. de Gironcoli, P. Delugas, R. A. DiStasio, A. Ferretti, A. Floris, G. Fratesi, G. Fugallo, R. Gebauer, U. Gerstmann, F. Giustino, T. Gorni, J. Jia, M. Kawamura, H. Y. Ko, A. Kokalj, E. Küçükbenli, M. Lazzeri, et al., *J. Phys.: Condens. Matter* **2017**, *29*, 465901.
- [56] P. Giannozzi, S. Baroni, N. Bonini, M. Calandra, R. Car, C. Cavazzoni, D. Ceresoli, G. L. Chiarotti, M. Cococcioni, I. Dabo, A. D. Corso, S. de Gironcoli, S. Fabris, G. Fratesi, R. Gebauer, U. Gerstmann, C. Gougoassis, A. Kokalj, M. Lazzeri, L. Martin-Samos, N. Marzari, F. Mauri, R. Mazzarello, S. Paolini,

- A. Pasquarello, L. Paulatto, C. Sbraccia, S. Scandolo, G. Sclauzero,
A. P. Seitsonen, et al., *J. Phys.: Condens. Matter* **2009**, *21*, 395502.
- [57] J. P. Perdew, K. Burke, M. Ernzerhof, *Phys. Rev. Lett.* **1996**, *77*, 3865.
- [58] P. E. Blöchl, O. Jepsen, O. K. Andersen, *Phys. Rev. B* **1994**, *49*, 16223.
- [59] G. Kresse, D. Joubert, *Phys. Rev. B* **1999**, *59*, 1758.
- [60] D. J. Evans, B. L. Holian, *J. Chem. Phys.* **1985**, *83*, 4069.
- [61] V. L. Deringer, A. L. Tchougréeff, R. Dronskowski, *J. Phys. Chem.* **2011**, *115*, 5461.
- [62] R. Dronskowski, P. E. Bloechl, *J. Phys. Chem. A* **1993**, *97*, 8617.
- [63] H. J. Monkhorst, J. D. Pack, *Phys. Rev. B* **1976**, *13*, 5188.